Occurrence of ferroan trevorite within olivine megacrysts of the MORB from Southern East Pacific Rise

S. K. Pandey, J. P. Shrivastava* and G. S. Roonwal

Department of Geology, University of Delhi, Delhi 110 007, India

We report ferroan trevorite (NiO = 16.22 and FeO$_{(Total)}$ = 83.06) mineral phase that occurs within the olivine megacrysts of the mid-Ocean ridge basalt from the Southern East Pacific Rise, indicative of Ni-enrichment, possibly linked to the heterogeneity in the lower mantle.

Keywords: Ferroan trevorite, mantle heterogeneity, Ni-enrichment, olivine megacrysts.

THE Southern East Pacific Rise (SEPR) represents a super-fast (up to 16 cm/yr) spreading axis[1] that forms the Pacific and Nazca Plate boundaries. Previous studies[2–7] on this axis pointed out large-scale mantle heterogeneity below the area (Figure 1 a). Samples were collected on-board the research vehicle Sonne during the German expedition, GEOMETEP IV. The present work is related to major and trace (Ni and Cr) elements geochemistry, and optical and electron probe micro analysis (EPMA) of samples to understand nature of the mantle heterogeneity below the SEPR. Thus, the work is focused on a large transect (6°S–26°S) extending along the axis of the SEPR. In all, 59 samples were collected from the thirty sampling sites 122D to 412G over this transect. Petrography and modal analyses were carried out for 37 samples (Table 1). For the latter, an Image Analyzer (Leica Make, Qwin DMRX model) was used. It is observed that the high modal olivine (>6.73%) values are restricted to a group of six samples from 128G and all sample from 122D, 141G and 154D sampling sites. Samples having unusually high olivine (Table 2) content reflecting primitive nature are significant and have been considered for the EPMA.

Physical and optical properties of the constituent mineral phases along with the modal data are presented in Table 1. A microscopic study revealed the presence of olivine megacrysts with interspersed spinel grains (Figure 2 a). Relict, highly deformed, cubic, sub-rounded to rounded spinel grains that lie within the olivine megacrysts show high relief. Major oxide data (Table 3) for these samples (obtained by XRF analysis) show high (>7%) MgO values. These samples also represent high (>60) values for their Mg number. The data when plotted as a total alkali vs silica (TAS) diagram (Figure 3), show that these are basalt and basaltic andesite. Calculated norms also revealed the same result (Table 3). The data obtained from these samples show high Ni values

*For correspondence. (e-mail: jpshrivastava.du@gmail.com)
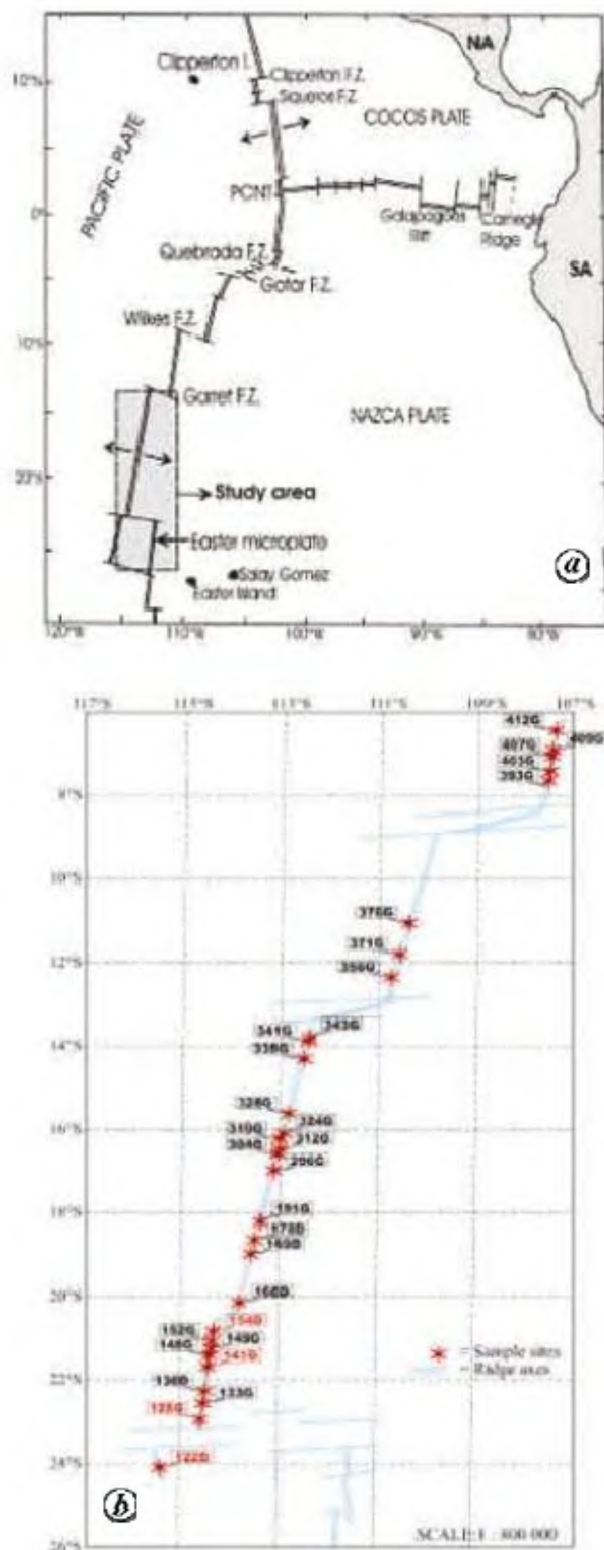
Figure 1. Location map of the study area in the South Pacific Ocean (modified after Naar and Hey[18]). *a*, The double lines indicate ridge axis, whereas the single line cutting the ridge axis is the offset. Opposite arrows show the direction of movement of the plates. *b*, Ridge axis of the East Pacific Rise (EPR), and positions of the sample recovery. SA, South America; NA, North America; FZ, Fracture zone and PCNT, Pacific Cocos Nazca Triple Junction; ===, EPR Ridge Axis; *, Sample location.

Table 1. Position, depth of recovery, macro and microscopic properties and major mineral components observed under a microscope of mid-Ocean ridge basalt (MORB) samples collected from southern East Pacific Rise (SEPR)

Sample	Depth (m)	Location	Megascopic character	Microscopic character
122D, 122D$_3$, 122D$_4$, 122D$_5$ and 122D$_6$	3244	26°6.223′S 110°31.340′W	Fresh massive basalt; surface is hydro thermally altered. Phenocrysts of plagioclase are visible on cutting side	Porphyritic; microcrysts less abundant and randomly oriented; groundmass occupied by glass, cpx and opaque.
128G$_1$, 128G$_2$, 128G$_3$, 128G$_4$, 128G$_7$ and 128G$_8$	3011–3044	22°59.350′S 114°30.769′W	Massive basalt; part of the surface is glassy; least hydrothermal alteration at surface.	Porphyritic; crystals randomly oriented; plagioclase crystals show both simple and lamellar twinning.
133G$_1$, 133G$_5$,	2910–2925	22°39.515′S 114°29.677′W	Massive basalt; glass is seen at upper end, alteration effect is visible and plagioclase is dominant.	Inequigranular; icrophencrysts mostly composed of plagioclase laths and olivine; groundmass consists entirely of glass.
136D$_1$	2914	22°15.348′S 114°27.216′W	Massive and compact basalt; convex upward; glass is seen on upper surface.	Phenocrysts composed of plagioclase of varying size, devitrification of glasses also visible.
141G$_1$, 141G$_2$	2900–2928	21°47.812′S 114°21.647′W	Massive basalt, plagioclase is distinct, thin film of alteration products.	Phenocrysts consist of euhedral crystals of plagioclase and are randomly oriented, glomero-porphyries visible.
148G$_2$, 148G$_3$, 148G$_4$	2797	21°4.41°S 114°16.745′W	Compact basalt plate, numerous small pits due to quenching.	Phenocrysts of euhedral plagioclase showing simple twinning, microcrysts of olivine/cpx/opx are scattered.
149G$_1$, 149G$_2$, 149G$_3$	2788	21°8.54′S 114°16.606′W	Massive basalt; thin veneer of glass, alteration at surface, numerous small pits are present indicating quenching effect.	Phenocrysts consist of lath-shaped and tabular plagioclase, devitrification of glasses is visible.
154D, 154D$_1$	2790–2810	21°02.285′S 114°13.197′W	Fine-grained, compact basalt, glassy at surface, plagioclases are distinct, few small pits are present, less alteration.	Phenocrysts of plagioclase and olivine are randomly oriented, zoning in plagioclase.
168D$_1$, 168D$_2$	2828–2838	20°4.965′S 113°42.153′W	Massive basalt; alteration at surface; presence of numerous small pits.	Phenocrysts and microcrysts of plagioclase are randomly oriented, devitrification of glasses visible.
169F$_2$	2781	19°21.957′S 113°31.728′W	Small, compact, glassy basalt, alteration at surface.	Microcrysts of plagioclase are elongated, exhibiting flow structure.
178D$_2$	2800	18°52.115′S 113°26.507′W	Fine-grained basalt, small glassy proportion, alteration at surface.	Microcrysts of plagioclase are abundant and randomly oriented.
338G	2624	14°26.851′S 112°35.942′W	Massive basalt, upper surface glassy, alterations at surface, some small pits are present.	Porphyritic with microcrysts of plagioclase; devitrified glasses visible.
412G, 412G$_2$	2637–2670	14°04.295′S 112°30.712′W	Massive basalt, upper surface glassy; minor alteration visible.	Exhibiting vitrophyric texture; devitrification of glasses visible.

G, Grab samples; D, Dredge samples; F, Underwater photographic unit sample.
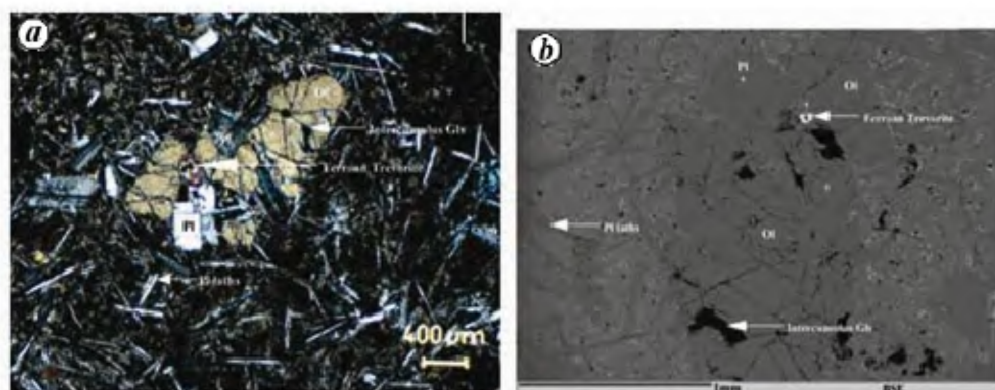
Figure 2. Photomicrograph of mid-Oceanic ridge basalt (MORB) sample from 128G under crossed nicol. *a*, Orthocumulus megacryst of olivine along with intercumulus ferroan trevorite. *b*, Back scattered electron image of the thin section in opposite orientation. Groundmass phases are plagioclase microlaths, glass and iron oxide. + indicates sites of EPMA analysis; Ol, Olivine; Pl, Plagioclase; Gls, Glass.

Table 2. Modal data (in vol%) for mineral phases and glass as determined in MORB samples from the SEPR

| Sample	Ol	Pl (P)	Pl (G)	Py	Gls	Spl	GC
122D	3.9	3.93	14.23	1.09	74.89	1.96	–
122D$_3$	12.43	4.08	19.5	1.64	59.32	3.03	–
122D$_4$	3.28	5.09	27.2	4.65	55.5	3.29	–
122D$_5$	3.26	2.23	35.04	–	57.53	1.94	–
122D$_6$	3.82	7.38	21.3	4.7	60.19	1.61	–
128G$_1$	9.08	31.36	–	0.91	50.39	8.26	–
128G$_2$	6.03	28.28	–	0.35	64.49	0.84	–
128G$_3$	4.82	14.47	–	2.36	76.87	1.49	–
128G$_4$	6.73	34.08	–	3.04	53.02	3.14	–
128G$_7$	4.81	32.33	0.93	–	55.31	6.62	–
128G$_8$	3.98	25.54	–	0.68	64.06	6.42	–
133G$_1$	2.55	7.26	24.35	–	51.4	14.44	–
133G$_5$	1.63	2.55	10.57	–	67.42	5.34	12.49
136D$_1$	0.38	7.23	0.63	–	92.14	–	–
141G	8.07	18.06	–	2.54	62.45	8.42	–
141G$_3$	4.75	18.14	3.6	0.43	62.47	7.56	3.05
148G$_2$	0.93	7.42	3.56	–	85.86	2.23	–
148G$_3$	0.97	9.23	3.49	–	84.86	3.19	–
148G$_4$	0.93	5.51	2.56	–	85.86	2.23	–
149G$_1$	–	–	2.62	–	94.54	2.84	–
149G$_2$	–	0.99	2.37	–	92.91	3.73	–
149G$_3$	–	1.06	3.28	–	92.82	2.84	–
154D	0.86	6.54	0.73	–	87.34	4.53	–
154D$_1$	11.1	19.2	–	3.49	59.52	5.27	0.91
168D$_1$	2.09	5.07	–	–	86.17	4.17	2.5
168D$_2$	5.52	4.07	10.23	–	71.58	4.87	3.73
169F$_2$	–	4.17	–	–	95.29	0.54	–
178D$_2$	1.58	8.45	17.21	0.32	67.82	4.02	0.92
338G	1.94	17.09	–	–	76.98	3.99	–
412G	–	3.29	–	–	96.01	0.37	0.33
412G$_2$	2.21	4.89	–	1.27	86.85	5.05	–

Ol, Olivine; Pl (P), Plagioclase (Phenocryst); Pl (G), Plagioclase (groundmass); Py, Pyroxene; Gls, Glass; Spl, Spinel; GC, Gas cavity; –, represents very low (0.001%) amount of mineral/gas cavity.
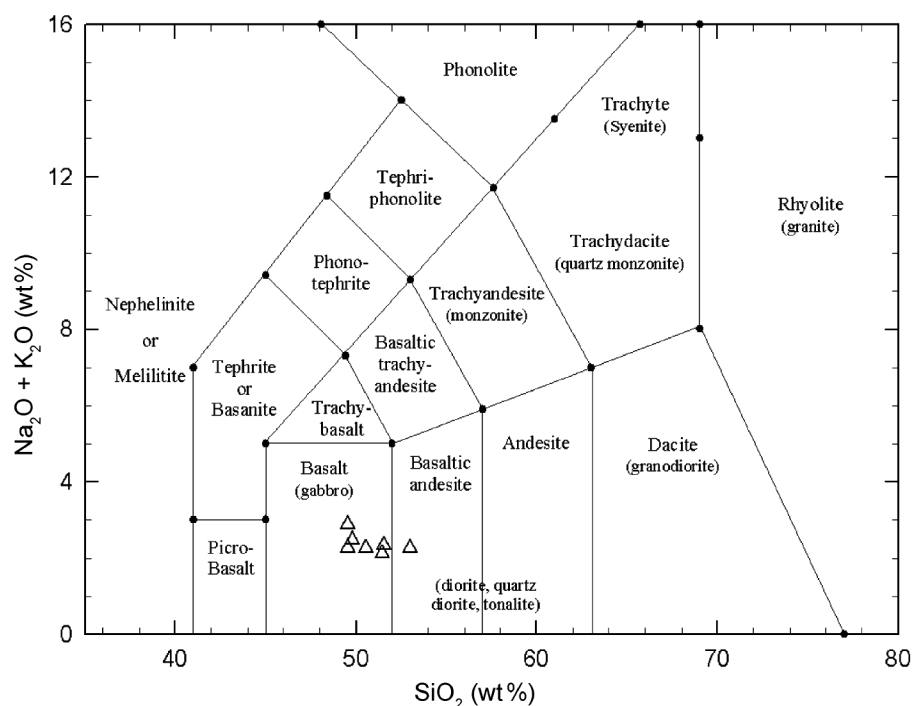
Figure 3. TAS diagram according to the IUGS classification scheme showing data plots for MORB samples (based on data in Table 3).

Table 3. Major oxides (in wt%), CIPW norms and calculated parameters for fresh samples from SEPR

Sample	$122D_3$	$128G_3$	$128G_4$	$128G_7$	$128G_8$	$141G_1$	$154F_1$
Major oxides (wt%)							
SiO_2	49.78	50.55	51.51	49.52	52.97	49.52	51.45
TiO_2	1.47	1.11	1.13	0.9	1.59	2.02	1.21
Al_2O_3	10.7	14.42	13.6	12.5	13.45	11.19	10.58
Fe_2O_3 (Total)	12.41	9.59	9.84	10.92	10.17	15.17	12.06
MnO	0.02	0.16	0.16	0.16	0.16	0.21	0.18
MgO	9.43	8.76	7.98	10.18	7.73	7.6	9.38
CaO	12.35	12.39	12.94	11.71	10.13	10	10.96
Na_2O	2.3	2.16	2.31	2.24	2.03	2.83	2.1
K_2O	0.18	0.11	0.04	0.02	0.23	0.06	0.03
P_2O_5	0.2	0.07	0.05	0.05	0.09	0.12	0.06
LOI	0.52	0.16	–	0.76	–	0.42	1.33
Total	99.36	99.48	99.56	98.96	98.55	99.14	99.22
CIPW norm (wt%)							
Q	–	0.13	2.183	–	8.254	2.58	5.353
Or	1.087	0.662	0.236	0.118	1.389	0.36	0.183
Ab	19.902	18.556	19.784	19.453	17.575	24.514	18.286
An	18.755	29.768	26.952	24.623	27.528	18.072	19.914
Di	34.6	26.028	30.486	27.789	18.822	25.887	28.651
Hy	15.797	20.397	14.998	20.302	19.923	17.209	19.528
Ol	3.723	–	–	0.886	–	–	–
Mt	2.807	2.153	3.069	4.954	3.207	7.165	5.576
Il	2.855	2.14	2.173	1.755	3.09	3.928	2.365
Ap	0.473	0.164	0.118	0.118	0.213	0.285	0.144
Calculated parameters							
$Mg^{\#}$	63.978	68.105	67.107	72.654	65.661	59.278	69.066
FeO^T/MgO	1.184	0.985	1.11	0.965	1.184	1.796	1.157
Salic	39.744	49.116	49.155	44.194	54.746	45.526	43.736
Femic	48.276	42.932	41.756	49.344	39.543	45.941	48.918
CI	77.898	78.712	80.473	82.154	65.741	63.97	76.06
DI	20.989	19.348	22.203	19.571	27.218	27.454	23.822
SI	40.529	44.228	41.149	45.046	39.931	30.864	41.255
AR	1.241	1.185	1.194	1.206	1.212	1.316	1.219
Rock type	B, subal	B, subal	BA	B, subal	BA	B, subal	BA

D, Dredge sample; G, Grab sample; F, Photographic sample; Fe_2O_3 (total), total iron expressed as Fe_2O_3; FeO^T, total iron expressed as FeO; $Mg^{\#}$, $100\ Mg^{+2}/(Mg^{+2} + Fe^{+2})$, atomic; Salic, Sum of salic normative minerals; Femic, Sum of femic normative minerals; CI, Crystallization index; DI, Differentiation index; SI, Solidification index; AR, Alkalinity ratio; B subal, Subalkalic basalt; BA, Alkali basalt. Rock types presented based on total alkalis vs silica diagram[19–21]. CIPW norms calculated[22] on anhydrous 100% adjusted basis, using Fe_2O_3/FeO ratio[23].
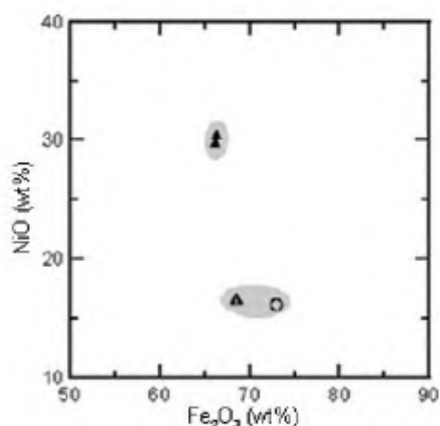
Figure 4. Bivariate data plot for intercumulus spinel and its chemical correlation with ferroan trevorite. O, Ferroan trevorite (present data); ▲, Trevorite and △, Ferroan trevorite (published data[9,10]).

(144–1037; averaged 375 ppm) compared to the published data on southern[4] as well as northern[8] EPR.

For microprobe analysis, sections were polished and coated with carbon. Wavelength-dispersive EPMA analysis was carried out using CAMECA SX100 at the Indian Bureau of Mines, Nagpur. Back scattered electron (BSE) images (Figure 2 b) were obtained at high magnification. An acceleration voltage of 15 kV and a beam diameter of 1 μm were used with a live counting time of 20 s. CuK_{α} X-ray emission lines of all the elements were used for calibration. International standards were used for the present analysis and precision was maintained to better than 2%. The ZAF data-reduction program was used to obtain oxide concentrations. In all, nine samples were selected for the analysis of spinel and olivine megacrysts. Analysis was performed in a point mode and 42 points were ana-

Table 4. EPMA data (wt%) for ferroan trevorite and olivine megacrysts obtained form the present investigation compared with the published values[9-11] of ferroan trevorite and trevorite

Oxide	Present data				Published data			
	1	2	3	4	5 (ref. 9)	6 (ref. 9)	7 (ref. 10)	8 (ref. 11)
SiO_2	–	–	41.72	40.68	0.66	0.47	1.4	0.36
TiO_2	0.05	0.05	–	0.08	n.d.	n.d.	n.d.	n.d.
Al_2O_3	0.04	0.04	0.1	0.55	0.03	0.00	0.00	0.22
Fe_2O_3	n.d.	73.04*	n.d.	n.d.	68.51	68.49	66.24	66.33
FeO	n.d.	17.33*	n.d.	n.d.	13	12.99	1.96	n.d.
FeO*	83.06	0.00	12.18	12	n.d.	n.d.	n.d.	n.d.
MnO	–	–	0.19	0.22	0.00	0.00	0.00	0.04
MgO	–	–	45.99	46.8	0.07	0.03	0.24	0.03
CaO	0.04	0.04	0.32	0.37	0.04	0.04	–	0.65
K_2O	–	–	–	0.03	n.d.	n.d.	n.d.	n.d.
Na_2O	–	–	–	–	n.d.	n.d.	n.d.	n.d.
Cr_2O_3	–	–	0.07	0.05	n.d.	n.d.	n.d.	0.37
NiO	16.22	16.22	0.09	0.16	16.75	16.6	29.71	30.42
CoO	n.d.	–	n.d.	n.d.	0.32	0.32	0.00	0.43
H_2O	n.d.	–	n.d.	n.d.	n.d.	n.d.	0.36	n.d.
Total	99.41	106.73	100.66	100.91	99.38	98.94	99.91	98.85

Number of cations calculated on the basis of 32 oxygen atoms for spinel and number of cations calculated on the basis of four oxygen atoms for olivine

Si	–	–	1.032	1.006	0.204	0.146	0.433	0.113
Ti	0.015	0.011	–	0.001	n.d.	n.d.	n.d.	n.d.
Al	0.018	0.014	0.003	0.016	0.011	0.00	–	0.082
Fe^{2+}	n.d.	4.210	n.d.	n.d.	3.363	3.381	0.505	n.d.
Fe^{3+}	n.d.	15.964	n.d.	n.d.	15.947	16.042	15.414	15.714
Fe^{total}	26.879	–	0.221	0.215	n.d.	n.d.	n.d.	n.d.
Mn	–	–	0.004	0.005	–	–	–	0.11
Mg	–	–	1.695	1.725	0.032	0.014	0.111	0.014
Ca	0.017	0.012	0.008	0.01	0.013	0.013	–	0.219
K	–	–	–	0.001	n.d.	n.d.	n.d.	n.d.
Na	–	–	–	–	n.d.	n.d.	n.d.	n.d.
Cr	–	–	0.001	0.001	n.d.	n.d.	n.d.	0.092
Ni	5.048	3.789	0.002	0.03	4.167	4.156	7.396	7.703
Co	n.d.	–	n.d.	n.d.	0.079	0.080	–	0.109
Total	31.976	24.000	2.966	3.010	23.816	23.832	23.859	24.156

The present data on ferroan trevorite and their stoichiometrically calculated[12] values are shown in columns 1 and 2 respectively. Data for the margin and core of the olivine megacrysts, hosting ferroan trevorite are shown in columns 3 and 4. Published trevorite and ferroan trevorite data and their mineral formulae are given in columns 5–8. n.d., Not determined; –, not traced; *, Fe^{2+} and Fe^{3+} values calculated based on stoichiometry.

lysed for major and few trace elements (Ni and Cr) of interest. The average EPMA data are presented in Table 4.

EPMA of all the nine thin sections revealed the presence of ferroan trevorite. The microprobe data (Table 4) for Southern EPR samples were compared with the published values[9-11] available on trevorite and ferroan trevorite minerals. It is observed that the olivine megacrysts hosting spinel grains and intercumulus melt are rich in Mg, but poor in Ni. The Mg-rich olivine megacrysts represent a primitive composition of basalt, formed at the initial stage of melt fractionation, possibly at a relatively high temperature and greater depth. Intercumulus melt present within the olivine megacryst (Figure 2 a) is post-formational and appears black in the BSE image (Figure 2 b). Deformation in the olivine grains may have taken place during their upward movement. The intercumulus spinel grains appear white in the BSE image (Figure 2 b). When analysed these grains show unusually high values of NiO (16.22 wt%) and total FeO (83 wt%). However, other oxides present in these grains are in traces. For comparison, the present spinel data were recalculated based on stoichiometry[12], to obtain ferrous and ferric iron contents. The data were then plotted over a bivariate diagram (Figure 3) along with the published data on trevorite and ferroan trevorite ($NiFe^{3+}O_4$). It has been observed that the present data plots lie close to the ferroan trevorite, but fall away from the trevorite compositional field, indicating close chemical correlation with the ferroan trevorite (Figure 4).

The olivine formed from the primary melt[13] usually contains ~0.4 (wt%) of NiO, which is due to the fact that the olivine present in the lherzolite field of the upper mantle also contains uniform NiO content to the level of ~0.4 wt%. However, relatively much lower NiO (~0.09–0.16%) values have been observed in the olivine megacrysts of this area (Table 4). These are in contrast with the published values[13]. This is justified by the fact that the partial melting started[14] in the stability field of spinel peridotite (lherzolite) at a depth of 30–75 km and at 10~20 kbar. In this stability field, the widespread, relict-type spinel grains were the first minerals to crystallize out from the melt. In the MORB, during the convective movement of the magma, formation of spinel prior to olivine has been suggested[15]. The Ni ions segregated from the melt[16]. However, possibility of such a mechanism in the SEPR has not been understood. In this context, it is highly likely that the Ni ions were segregated and later exhausted in the formation of ferroan trevorite. Therefore, a large number of Ni ions were consumed prior to the nucleation of olivine, leaving behind the olivine phase is depleted in Ni ions. Thus, the formation of ferroan trevorite has been suggested.

It has been already reported[16] that the terrestrial trevorite originated from the oxidation of spinel and further that the enrichment of Ni resulted from the heterogeneity of the lower mantle when it ascended to the earth's surface as a result of convective processes. It is thus concluded that the ferroan trevorite, a characteristic meteoritic mineral[17], which usually occurs in ultramafic rocks or in Ni ores[8], identified from the MORB of the SEPR, ascribed to the process of segregation of Ni ions in the heterogeneous magma, that too in the lower part of the mantle within the stability field of spinel peridotite or lherzolite. The present finding of ferroan trevorite on the ridge axis is significant and its unusual presence is explained by the heterogenetic character of the source magma in terms of segregation of Ni ions.

1. Detrick, R. S., Harding, A. J., Kent, G. M., Orcutt, J. A., Mutter, J. C. and Buhl, P., Seismic structure of the southern East Pacific Rise. *Science*, 1993, **259**, 499–503.
2. Sinton, J. M., Smaglik, S. M., Mahoney, J. J. and Macdonald, K. C., Magmatic processes at superfast spreading mid-Ocean ridges: glass compositional variations along the east pacific rise 13°–23°S. *J. Geophys. Res.*, 1991, **96**, 6133–6156.
3. Mahoney, J. J., Sinton, J. M., Kurz, M. D., Macdougall, J. D., Spencer, K. J. and Lugmair, G. M., Isotope and trace element characteristics of a superfast spreading ridge: East Pacific Rise, 13–23°S. *Earth Planet. Sci. Lett.*, 1994, **121**, 173–193.
4. Bach, W., Hegner, E., Erzinger, J. and Satar, M., Chemical and isotopic variation along the superfast spreading East Pacific Rise from 6° to 30°S. *Contrib. Mineral. Petrol.*, 1994, **116**, 365–380.
5. Roonwal, G. S., Marchig, V., Rosch, H., Milovanovic, D. and Bellieni, G., A gabbroic xenolith in recent mid-oceanic ridge basalt from the East Pacific Rise at 14°S. *Curr. Sci.*, 1996, **70**, 724–729.
6. Processes and fluxes on a superfast spreading rise – SEPR, Ridge Inter-Disciplinary Global Experiments (RIDGE 2000), Workshop Report, July 1996; http://www.ridge2000.org/science/downloads/newsletter/R2Knews
7. Progress and plan meeting report, Ridge Inter-Disciplinary Global Experiments, RIDGE 2000, April 2006; http://www.ridge2000.org/science/iss/epr
8. Sims, K. W. W. *et al.*, Aberrant youth: chemical and isotopic constraints on the origin of off-axis lavas from the East Pacific Rise, 9°–10°N. *Geochem. Geophys. Geosyst.* (*G³*), 2003, **4**, 1–27.
9. De Waal, S. A., Nickel mineral from Barberton, South Africa: I. Ferroan Trevorite. *Am. Mineral.*, 1969, **54**, 1204–1208.
10. De Waal, S. A., Nickel mineral from Barberton, South Africa: V. Trevorite redescribed. *Am. Mineral.*, 1972, **27**, 1527–1530.
11. Deer, W. A., Howie, R. A. and Zussman, J., *Rock Forming Minerals Vol. 5, Non-silicates*, William Clowes and Sons Ltd, London, 1962, 1st edn, p. 371.
12. Droop, G. T. R., A general equation for estimating Fe^{3+} concentrations in ferromagnesian silicates and oxides from microprobe analyses, using stoichiometric criteria. *Mineral. Mag.*, 1987, **51**, 431–435.
13. Sato, H., Nickel content of basaltic magmas: identification of primary magmas and a measure of the degree of olivine fractionation. *Lithos*, 1977, **10**, 112–120.
14. Best, M. G. and Christiansen, E. H., *Igneous Petrology*, Blackwell, Oxford, 2001, p. 458.
15. Ray, D., Iyer, S. D., Banerjee, R., Misra, S. and Widdowson, M., A petrogenetic model of basalts from the Northern Central Indian Ridge: 3°–11°S. *Acta Geol. Sin.*, 2007, **18**, 99–112.
16. Muravyeva, N. S. and Senin, V. G., Trevorite in pyroxenite nodules from the Tokinsky Stanovik Mountains (ENE prolongation of Baikal rift zone). *Mineral. Mag.*, 1993, **57**, 171–173.
17. Schmidt, R. A. and Keil, K., Electron microprobe study of spherules from Atlantic Ocean sediments. *Geochim. Cosmochim. Acta*, 1966, **30**, 471–474.
18. Naar, D. F. and Hey, R. N., Tectonic evolution of Ester Microplate. *J. Geophys. Res.*, 1991, **96**, 7961–7993.
19. Le Bas, M. J., Le Maitre, R. W., Streckeisen, A. and Zanettin, B., A chemical classification of volcanic rocks based on the total alkali-silica diagram. *J. Petrol.*, 1986, **27**, 745–750.
20. Le Bas, M. J., Nephelinitic and basanitic rocks. *J. Petrol.*, 1989, **30**, 1299–1312.
21. Le Bas, M. J., IUGS reclassification of high – Mg and picritic volcanic rocks. *J. Petrol.*, 2000, **41**, 1467–1470.
22. Verma, S. P., Torres-Alvarado, I. S. and Sotelo-Rodríguez, Z. T., SINCLAS: Standard igneous norm and volcanic rock classification system. *Comput. Geosci.*, 2002, **28**, 711–715.
23. Middlemost, E. A. K., Iron oxidation ratios, norms and the classification of volcanic rocks. *Chem. Geol.*, 1989, **77**, 19–26.